

We are IntechOpen, the world's leading publisher of Open Access books Built by scientists, for scientists

6,900

Open access books available

186,000

International authors and editors

200M

Downloads

Our authors are among the

154

Countries delivered to

TOP 1%

most cited scientists

12.2%

Contributors from top 500 universities



WEB OF SCIENCE™

Selection of our books indexed in the Book Citation Index
in Web of Science™ Core Collection (BKCI)

Interested in publishing with us?
Contact book.department@intechopen.com

Numbers displayed above are based on latest data collected.
For more information visit www.intechopen.com



Fundamentals and Applications of Quantum Limited Optical Imaging

Warwick P. Bowen¹, Magnus T. L. Hsu¹ and Jian Wei Tay²

¹*School of Mathematics and Physics, University of Queensland, QLD 4072*

²*Physics Department, University of Otago, Dunedin*

¹*Australia*

²*New Zealand*

1. Introduction

The field of optical imaging is focussed on techniques to extract useful information about a physical system from the spatial structure of light. There are two main themes to research in this field, the resolving of previously unknown structures ranging in size from microns in microscopy to distant galaxies in astronomical telescopes; or if the structure is selected from an *a priori* known set, then its unique discrimination, such as in data read-out from a CD or DVD. In general, both types of imaging involve the collection and focusing of light after interaction with the object. However, the process of information extraction can be quite different. In resolving an unknown structure, a full two dimensional image is usually desired. Here, the metric of success is generally the resolution of the final image. In most cases diffraction is the key concern, presenting the diffraction limit to the resolution of the final image as approximated by Abbe (Born & Wolf, 1999). There are ways to overcome this limit, such as by utilising non-linearities (Hell *et al.*, 2009), or using metamaterials (Pendry, 2000) to form so called superlenses, and this is a vibrant and growing area of research.

The focus of this Chapter, however, is on the second theme of imaging, discrimination between a set of known structures. As we will see, this form of imaging is important, not only for read-out of information from data storage devices, but also in other areas such as microscopy (Fabre *et al.*, 2000; Tay *et al.*, 2009) and satellite navigation (Arnon, 1998; Nikulin *et al.*, 2001). In structure discrimination, the goal is not to achieve a two dimensional image, but rather to generate a signal which unambiguously distinguishes each element of the set. Hence, the diffraction limit and other constraints on imaging resolution are no longer the primary concern, but rather the signal-to-noise ratio with which the discrimination may be performed. To maximise the signal the optical measurement must be matched carefully to the set of structures to be discriminated; whereas the noise typically comes from electronic, environmental, and optical sources. Much engineering effort has been applied to minimising the noise sources for important imaging systems; however, fundamentally the quantisation of light imposes the quantum noise limit (QNL) which is outside of engineering control. In this Chapter we consider a general imaging system, and show how the optical mode carrying full signal information may be determined. We introduce spatial homodyne detection (Beck, 2000; Hsu *et al.*, 2004) as a method to optimally extract this signal, showing

Source: Advances in Lasers and Electro Optics, Book edited by: Nelson Costa and Adolfo Cartaxo, ISBN 978-953-307-088-9, pp. 838, April 2010, INTECH, Croatia, downloaded from SCIYO.COM

how the QNL to measurement sensitivity may be determined and even surpassed using non-classical states of light. We illustrate the implications of these techniques for two key imaging systems, atomic force microscopy (Binning *et al.*, 1985; Fabre *et al.*, 2000) and particle tracking in optical tweezers (Block, 1992; Tay *et al.*, 2009); comparing optimal spatial homodyne based signal extraction to the standard extraction methods used in such systems today.

2. Quantum formalism for optical measurements

The field of optical measurements has progressed significantly, with photo-detection techniques advancing from the use of the photographic plate in the 19th century to the semiconductor-based photodetectors commonly encountered today. One is now able to measure with high accuracy and speed, the range of parameters that describe an optical field. For example, the amplitude and phase quadratures, the Stokes polarisation parameters, and the transverse spatial profile that are commonly used to parameterise the optical field (Walls & Milburn, 1995). These parameters can be measured and quantified using a range of detection techniques such as interferometry, polarimetry and beam profiling (Saleh & Teich, 1991). However, experimentally measured values for these parameters are estimates due to the presence of classical and quantum noise, and detection inefficiencies.

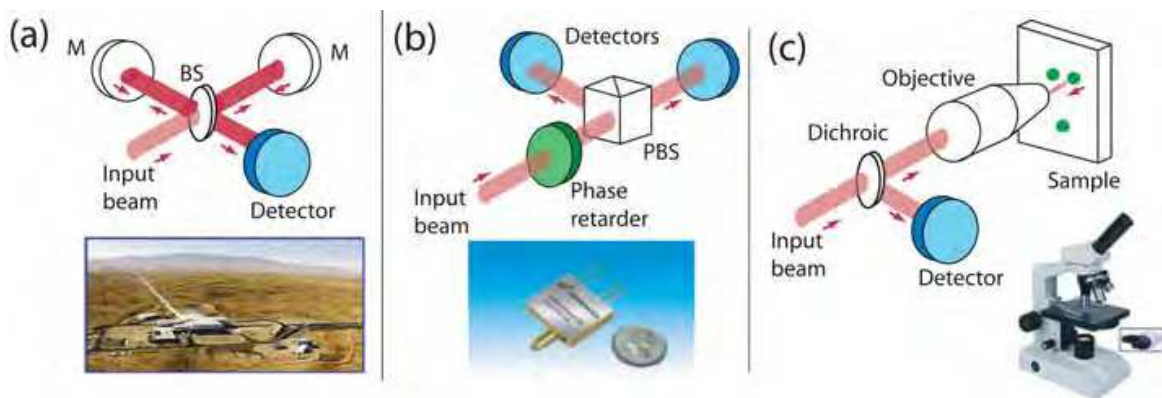


Fig. 1. Schematics of (a) a Michelson interferometer with an inset photo of the Laser Interferometer Gravity-wave Observatory (LIGO), (b) a polarimeter with inset photo of an on-chip polarimeter, and (c) an optical microscope with an inset photo of an optical microscope. M: mirror, BS: beam-splitter and PBS: polarising beam-splitter.

Fig. 1 shows examples of techniques used for the measurement of (a) amplitude and phase quadratures (Slusher *et al.*, 1985), (b) polarization (Korolkova & Chirkin, 1996) and (c) spatial variables (Pawley, 1995). Fig. 1 (a) shows a Michelson interferometer whereby an input field is split using a beam-splitter, followed by propagation of the two output fields through different paths with an effective path difference. These two fields are then interfered to produce an output interference signal. Depending on the effective path difference, destructive or constructive interference is obtained at the output of the interferometer. Variations of this technique include the Mach-Zehnder (Mach, 1892; Zehnder, 1891) and Sagnac (Sagnac, 1913) interferometers. A polarimeter is shown in Fig. 1 (b), where an input field is phase retarded and the different polarisation components of the input field are separated using a polarization beam-splitter. A measurement of the intensity difference

between the different polarization components provides information on the Stokes variables that characterise the polarization phase space (Bowen *et al.*, 2002). Interferometry and polarimetry are essentially single spatial mode techniques, since the spatial discrimination of the field structure cannot be characterized with these techniques. In order to reach their measurement sensitivity limits, classical noise sources have to be reduced (or eliminated) sufficiently such that quantum noise becomes the dominant noise source. Consequently, optimal measurements of the amplitude and phase quadratures as well as the polarisation variables are obtained, with measurement sensitivity bounded at the QNL.

Measurements of the spatial properties of light are more complex, since multiple spatial modes are naturally involved. Therefore noise sources are no longer the sole consideration, with the modal selection and filtration processes also becoming critical. Fig. 1 (c) shows a schematic of an optical microscope, where a focused light field is used to illuminate and image a microscopic sample. Existing techniques to resolve the finer spatial details of an optical image include for example the filtration of different spatial frequency components via confocal microscopy (Pawley, 1995); or the collection of non-propagating evanescent modes that decay exponentially over wavelength-scales via near-field microscopy (Synge, 1928).

Here we are interested in the procedure of optimal parameter measurement, as shown in Fig. 2, whereby the detection system is tailored to optimally extract a specific spatial signal. An input field is spatially perturbed (i.e. a spatial signal is applied to the optical field, be it known or unknown), and the resultant field is detected. To be able to optimally measure the perturbation applied to the field, the relevant signal field components have to be identified and resolved.

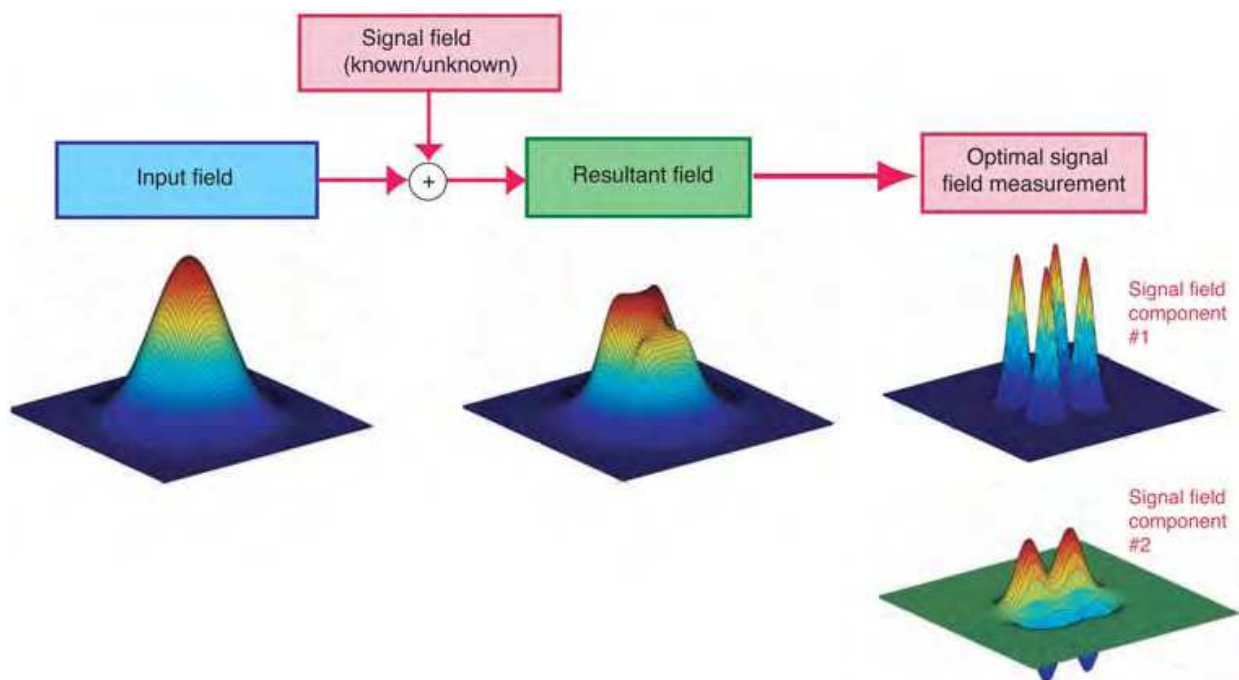


Fig. 2. The optimal parameter measurement procedure. An input field is perturbed by some known or unknown spatial signal and the resultant field is detected. Optimal measurements of the perturbation can be performed by identifying and resolving the relevant signal field components.

We now present a formalism for defining the quantum limits to measurements of spatial perturbations of an optical field. The spatial perturbation, quantified by parameter p is entirely arbitrary, and could for instance be the displacement or rotation of a spatial mode in the transverse plane (Hsu *et al.*, 2004; 2009), or the perturbation introduced by an environmental factor such as scattering from a particle within the field or atmospheric fluctuations.

In general, the optical field requires a full three dimensional description using Maxwell's equations (Van de Hulst, 1981). In systems where all dimensions are significantly larger than the optical wavelength, however, the paraxial approximation can usually be invoked and the field can be described using two dimensional transverse spatial modes in a convenient basis. The spatial quantum states of an optical field exist within an infinite dimensional Hilbert space, and may be conveniently expanded in the basis of the rectangularly-symmetric TEM_{mn} or circularly-symmetric LG_{nl} modes, with the choice of modal basis dependent on the spatial symmetry of the imaged optical field.

A field of frequency ω can be represented by the positive frequency part of the electric field operator $\tilde{\mathbf{E}}^+(\rho)e^{i\omega t}$. Following Tay *et al.* (2009), the transverse information of the field is described fully by the slowly varying field envelope operator $\tilde{\mathbf{E}}^+(\rho)$, given by

$$\tilde{\mathbf{E}}^+(\rho) = i\sqrt{\frac{\hbar\omega}{2\epsilon_0 V}} \sum_{j,m,n} \tilde{a}_{mn}^j \mathbf{u}_{mn}^j(\rho), \quad (1)$$

where $\rho = (x,y)$ is a co-ordinate in the transverse plane of the field, V is the volume of the optical mode, and the summation over the parameters j , m and n is given by

$$\sum_{j,m,n} \equiv \sum_{j \in \{x,y\}} \sum_{m=0}^{\infty} \sum_{n=0}^{\infty}. \quad (2)$$

The respective transverse beam amplitude function and the photon annihilation operator are given by $\mathbf{u}_{mn}^j(\rho)$ and \tilde{a}_{mn}^j , with polarisation denoted by the superscript j . The $\mathbf{u}_{mn}^j(\rho)$ mode functions are normalized such that their self-overlap integrals are unity, with the inner product given by

$$\begin{aligned} \langle \mathbf{u}_{mn}^j(\rho), \mathbf{u}_{m'n'}^{j'}(\rho) \rangle &= \int_{-\infty}^{\infty} [\mathbf{u}_{mn}^j(\rho)]^* \cdot \mathbf{u}_{m'n'}^{j'}(\rho) d\rho \\ &= \delta_{mm'} \delta_{nn'} \delta_{jj'}. \end{aligned} \quad (3)$$

An arbitrary spatial perturbation, described by parameter p , is now applied to the field. Eq. (1) can therefore be expressed as a sum of coherent amplitude components and quantum noise operators, given by

$$\begin{aligned} \tilde{\mathbf{E}}^+(\rho, p) &= i\sqrt{\frac{\hbar\omega}{2\epsilon_0 V}} \sum_{j,m,n} \tilde{a}_{mn}^j \mathbf{u}_{mn}^j(\rho, p) \\ &= i\sqrt{\frac{\hbar\omega}{2\epsilon_0 V}} \left[\alpha(p) \mathbf{v}(\rho, p) + \sum_{j,m,n} \delta \tilde{a}_{mn}^j \mathbf{u}_{mn}^j(\rho, 0) \right], \end{aligned} \quad (4)$$

where $\alpha(p)\mathbf{v}(\rho, p) = \sum_{j,m,n} \langle \tilde{a}_{mn}^j \rangle \mathbf{u}_{mn}^j(\rho, 0) = \sum_{j,m,n} \langle \tilde{a}_{mn}^j \rangle u_{mn}^j(\rho, 0) \hat{\mathbf{j}}$ being the coherent amplitude of mode $\mathbf{v}(\rho, p)$, and $\hat{\mathbf{j}}$ is the unit polarisation vector. From Eq. (4), one can then relate $\alpha(p)$ and $\mathbf{v}(\rho, p)$ to $\bar{\mathbf{E}}^+(\rho, p)$ by

$$\alpha(p) = \sqrt{\frac{2\epsilon_0 V}{\hbar\omega} \langle \bar{\mathbf{E}}^+(\rho, p), \bar{\mathbf{E}}^+(\rho, p) \rangle} \quad (5)$$

$$\mathbf{v}(\rho, p) = -iN_v \bar{\mathbf{E}}^+(\rho, p) \quad (6)$$

where $\bar{\mathbf{E}}^+(\rho, p) = \langle \tilde{\mathbf{E}}^+(\rho, p) \rangle$, and the normalization constant N_v is given by

$$\begin{aligned} N_v &= \langle \bar{\mathbf{E}}^+(\rho, p), \bar{\mathbf{E}}^+(\rho, p) \rangle^{-1/2} \\ &= \left[\iint_{-\infty}^{\infty} [\bar{\mathbf{E}}^+(\rho, p)]^* \cdot \bar{\mathbf{E}}^+(\rho, p) d\rho \right]^{-1/2}. \end{aligned} \quad (7)$$

The mean number of photons passing through the transverse plane of the field per second is given by $|\alpha(p)|^2$. We also assume, without loss of generality, that $\alpha(p)$ is real. The quantum noise operator carrying all of the noise on the field in mode $\mathbf{u}_{mn}(\rho) = \mathbf{u}_{mn}^j(\rho, 0)$ is given by $\delta \tilde{a}_{mn}^j = \tilde{a}_{mn}^j = \langle \tilde{a}_{mn}^j \rangle$.

In the limit of small estimate parameter p , we can take the first order Taylor expansion of the first bracketed term in Eq. (4), given by

$$\alpha(p)\mathbf{v}(\rho, p) \approx \alpha(0)\mathbf{v}(\rho, 0) + p \cdot \left. \frac{\partial[\alpha(p)\mathbf{v}(\rho, p)]}{\partial p} \right|_{p=0}, \quad (8)$$

where the first term on the right-hand side of Eq. (8) indicates that the majority of the power of the field is in the $\mathbf{v}(\rho, 0)$ mode. The second term defines the spatial mode $\mathbf{w}(\rho)$ corresponding to small changes in the parameter p , given by

$$\mathbf{w}(\rho) = \frac{1}{N_w} \left. \frac{\partial[\alpha(p)\mathbf{v}(\rho, p)]}{\partial p} \right|_{p=0}. \quad (9)$$

where N_w is the normalisation given by

$$N_w = \left\langle \left. \frac{\partial[\alpha(p)\mathbf{v}(\rho, p)]}{\partial p} \right|_{p=0}, \left. \frac{\partial[\alpha(p)\mathbf{v}(\rho, p)]}{\partial p} \right|_{p=0} \right\rangle^{-1/2}. \quad (10)$$

Notice that the first term in Eq. (8) is independent of p ; while the second term, and therefore the amplitude of mode $\mathbf{w}(\rho)$, is directly proportional to p . Therefore, by measuring the amplitude of mode $\mathbf{w}(\rho)$ it is possible to extract all available information about p . As a consequence, we henceforth term $\mathbf{w}(\rho)$ the *signal mode*.

3. Detection systems

Several techniques have been developed to experimentally quantify the amplitude of the signal mode. Here we discuss the three most common of such: array detection, split detection, and spatial homodyne detection, as shown in Fig. 3.

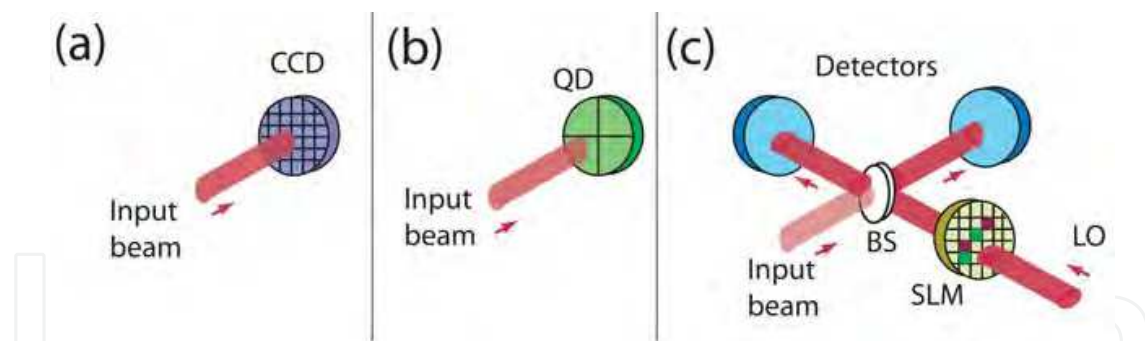


Fig. 3. Detection systems for the measurement of the spatial properties of the field. (a) Array, (b) split and (c) spatial homodyne detection systems. BS: beam-splitter, LO: local oscillator field, CCD: charge-coupled detector, QD: quadrant detector (four component split detector), SLM: spatial light modulator.

3.1 Array detection

As shown in Fig. 3 (a) array detectors in general consist of an $m \times n$ array of pixels each of which generates a photocurrent proportional to its incident optical field intensity. One subclass of array detectors is the ubiquitous charge-coupled device (CCD), which is the most common form of detector used for characterisation of the spatial properties of light beams. To the authors knowledge, the first quantum treatment of optical field detection using array detectors was given in Beck (2000). In this work Beck (2000) proposed the use of two array detectors with a local oscillator in a homodyne configuration to perform spatial homodyne detection. Such techniques will be discussed in detail in section 3.3. Quantum measurements with a simple single array were first considered later in papers by Treps, Delaubert and others (Treps *et al.*, 2005; Delaubert *et al.*, 2008). An ideal array detector consists of a two dimensional array of infinitesimally small pixels, each with unity quantum efficiency, and each registering the amplitude of its incident field with high bandwidth. However, realistic array detectors stray far from this ideal; with efficiencies generally around 70 % due both to the intrinsic inefficiency of the pixels and due to dead zones between pixels, complications in shift register readout, and bandwidth limitations¹. To date, all quantum imaging experiments utilising array detectors have been performed in the context of spatial homodyne detection. We therefore defer further discussion of these techniques to Section 3.3.

3.2 Split detection

One of the most important spatial parameters of an optical beam is the fluctuation of its mean position, commonly termed *optical beam displacement*, which provides extremely sensitive information about environmental perturbations such as forces exerted on microscopic systems (see Sections 4 and 5), mechanical vibrations, and air turbulence; as well as control information in techniques such as satellite navigation (Arnon, 1998; Nikulin *et al.*, 2001) and locking of optical resonators (Shaddock *et al.*, 1999), to name but a few. The most convenient means to measure optical beam displacement is through measurement on a split detector (Putman *et al.*, 1992; Treps *et al.*, 2002; 2003), as shown in Figure 3 (b). Such detectors are composed of two or more PIN photodetectors arranged side-by-side. So long

¹ For example, to achieve a typical quantum imaging detection bandwidth of 1 MHz, a 10-bit 10 megapixel CCD camera would require a total bit transfer rate of 100 T-bits/s.

as the optical field is aligned to impinge equally on the two photodetectors, and the optical beam shape is well behaved, the difference between the output photocurrents provides a signal proportional to the beam displacement. Furthermore, since only a pair of PIN photodiodes is used, both the efficiency and bandwidth issues related to array detection are easily resolved. The limitation of split detectors, however, is that they are restricted to measurement of a certain subset of signal modes, and therefore, in general will not be optimal for a given application (Hsu *et al.*, 2004). Here we derive the split detection signal mode following the treatments of Hsu *et al.* (2004) and Tay *et al.* (2009). The sensitivity achievable in the measurement of a general signal mode will be treated later in Section 3.4. The difference photocurrent output from a split detector can in general be written as

$$\Delta i_{\text{SD}} = i_{x<0} - i_{x>0} \quad (11)$$

$$= \frac{2\epsilon_0 V}{\hbar\omega} \left[\int_{-\infty}^{\infty} dy \int_{-\infty}^0 dx \tilde{\mathbf{E}}^{++} \cdot \tilde{\mathbf{E}}^+ - \int_{-\infty}^{\infty} dy \int_0^{\infty} dx \tilde{\mathbf{E}}^{++} \cdot \tilde{\mathbf{E}}^+ \right]. \quad (12)$$

This can be shown (Fabre *et al.*, 2000) to be equal to

$$\Delta i_{\text{SD}} = \alpha(p) \tilde{X}_f^+ \quad (13)$$

where $\tilde{X}_f^+ = \tilde{a}_f^+ + \tilde{a}_f$ is the amplitude quadrature operator of a *flipped mode* with mode intensity equal to that of the incident field but a π phase flip about the split between photodiodes. The transverse mode amplitude function of the flipped mode is given by

$$\mathbf{v}_f(\rho) = \begin{cases} \mathbf{v}(\rho, 0), & x \geq 0 \\ -\mathbf{v}(\rho, 0), & x < 0. \end{cases} \quad (14)$$

It is useful to separate the flipped mode amplitude quadrature operator into a coherent amplitude component

$$\alpha_f(p) = \alpha(p) \langle \mathbf{v}_f(\rho), \mathbf{v}(\rho, p) \rangle \quad (15)$$

which contains the signal due to the parameter p ; and a quantum noise operator $\delta\tilde{X}_f^+ = \tilde{X}_f^+ - \langle \tilde{X}_f^+ \rangle$ which places a quantum limit on the measurement sensitivity, so that

$$\Delta i_{\text{SD}} = \alpha(p) \left[2\alpha_f(p) + \delta\tilde{X}_f^+ \right]. \quad (16)$$

Hence, we see that split detection measures the signal and noise in a flipped version of the incident mode.

3.3 Spatial homodyne detection

Spatial homodyne detection was first proposed by Beck (2000) using array detectors, and was extended to the case of pairs of PIN photodiodes with a spatially tailored local oscillator field by Hsu *et al.* (2004). Spatial homodyne detection has the significant advantage over split detection in that the detection mode can be optimised to perfectly match the signal mode. The proposal of Beck (2000) has the advantage of allowing simultaneous extraction of multiple signals (Dawes *et al.*, 2001); whilst that of Hsu *et al.* (2004) allows high bandwidth

extraction of a single arbitrary spatial mode and is polarization sensitive allowing optimal measurements where the signal is contained within spatial variations of the polarisation of the field. Here, we explicitly treat local oscillator tailored spatial homodyne allowing the inclusion of polarisation effects. However, we emphasise that the two schemes are formally equivalent for single-signal-mode single-polarisation fields.

In a local oscillator tailored spatial homodyne, the input field is interfered with a much brighter local oscillator field on a 50/50 beam splitter; with the two output fields individually detected on a pair of balanced single element photodiodes, as shown in fig. 3 (c). The difference photocurrent between the two resulting photocurrents is the output signal. By shaping the local oscillator field, for example by using a set of spatial light modulators (SLM), an arbitrary spatial parameter of the input field can be interrogated. Spatial homodyne schemes of this kind have been shown to perform at the Cramer-Rao bound (Delaubert *et al.*, 2008), and therefore enable optimal measurement of any spatial parameter p .

The performance of a spatial homodyne detector can be assessed in much the same way as split detection in the previous section. Here we follow the approach of Tay *et al.* (2009), choosing a LO with a positive frequency electric field operator

$$\tilde{\mathbf{E}}_{\text{LO}}^+(\rho) = i\sqrt{\frac{\hbar\omega}{2\epsilon_0 V}} \left[\alpha_{\text{LO}} \mathbf{w}(\rho) + \sum_{j,m,n} \delta \tilde{a}_{mn, \text{LO}}^j \mathbf{u}_{mn}^j(\rho) \right] e^{i\phi}, \quad (17)$$

with the relative phase between the local oscillator and the input beam given by ϕ and local oscillator mode chosen to match the signal mode. The input beam described in Eq. (4) is interfered with the LO on a 50/50 beam splitter to give the output fields

$$\tilde{\mathbf{E}}_{\pm}^{\pm} = \frac{1}{\sqrt{2}} (\tilde{\mathbf{E}}^{\pm} \pm \tilde{\mathbf{E}}_{\text{LO}}^{\pm}) \quad (18)$$

where the subscripts + and - distinguish the two output fields. The photocurrents produced when each field impinges on an infinitely wide photodetector are given by

$$i_{\pm} = \frac{2\epsilon_0 V}{\hbar\omega} \int_{-\infty}^{\infty} \tilde{\mathbf{E}}_{\pm}^{\pm\dagger} \cdot \tilde{\mathbf{E}}_{\pm}^{\pm} d\rho \quad (19)$$

$$= \frac{2\epsilon_0 V}{\hbar\omega} \int_{-\infty}^{\infty} \frac{1}{2} (\tilde{\mathbf{E}}^{\pm} \pm \tilde{\mathbf{E}}_{\text{LO}}^{\pm})^{\dagger} \cdot (\tilde{\mathbf{E}}^{\pm} \pm \tilde{\mathbf{E}}_{\text{LO}}^{\pm}) d\rho, \quad (20)$$

which together with Eqs. (1), (3), and (17) yield the photocurrent difference

$$\begin{aligned} \Delta i_{\text{SH}} &= i_+ - i_- \\ &= \alpha_{\text{LO}} \int_{-\infty}^{\infty} \left[e^{-i\phi} [\mathbf{w}(\rho)]^* \cdot \sum_{j,m,n} \tilde{a}_{mn}^j \mathbf{u}_{mn}^j(\rho, p) + e^{i\phi} \mathbf{w}(\rho) \cdot \left(\sum_{j,m,n} \tilde{a}_{mn}^j \mathbf{u}_{mn}^j(\rho, p) \right)^{\dagger} \right] d\rho \\ &= \alpha_{\text{LO}} \left[e^{-i\phi} \sum_{j,m,n} \tilde{a}_{mn}^j \langle \mathbf{w}(\rho), \mathbf{u}_{mn}^j(\rho, p) \rangle + e^{i\phi} \left(\sum_{j,m,n} \tilde{a}_{mn}^j \langle \mathbf{w}(\rho), \mathbf{u}_{mn}^j(\rho, p) \rangle \right)^{\dagger} \right] \\ &= \alpha_{\text{LO}} \left[e^{-i\phi} \tilde{a}_w + e^{i\phi} \tilde{a}_w^{\dagger} \right] \\ &= \alpha_{\text{LO}} \tilde{X}_w^{\phi} \end{aligned} \quad (21)$$

where the annihilation operator \tilde{a}_w describes the input field component in mode $\mathbf{w}(\rho)$, and $\tilde{X}_w^\phi = e^{-i\phi}\tilde{a}_w + e^{i\phi}\tilde{a}_w^\dagger$ is the ϕ -angled quadrature operator of that component. The derivation above is valid in the limit that the local oscillator power is much greater than the signal power ($\alpha_{LO} \gg \langle \tilde{a}_w \rangle$), which enables terms that do not involve α_{LO} to be neglected.

An optimal estimate of the parameter p is obtained since the local oscillator mode is chosen to match the signal mode $\mathbf{w}(\rho)$, as shown in Eq. (21). The spatial homodyne detection scheme then extracts the quadrature of the signal mode with quadrature phase angle given by ϕ .

3.4 Quantifying the efficacy of parameter estimation

Eqs. (16) and (21) provide the output signal from both homodyne and split detection schemes. However we have yet to determine the efficacy of both schemes. To obtain a quantitative measure of the efficacy, we now introduce the signal-to-noise ratio (SNR) and sensitivity measures.

From Eq. (21) we see that the mean signal output from the spatial homodyne detector is given by

$$\langle \Delta i_{SH} \rangle = \alpha_{LO} \alpha_w(p) (e^{i\Delta\phi} + e^{-i\Delta\phi}), \tag{22}$$

where $\alpha_w(p) = \alpha(p) \langle \mathbf{w}(\rho), \mathbf{v}(\rho, p) \rangle$. The maximum signal strength occurs when the local oscillator and signal phases are matched, such that $\phi = 0$, and is given by

$$\langle \Delta i_{SH} \rangle = 2\alpha_{LO} \alpha_w(p). \tag{23}$$

The noise can be calculated straight-forwardly, and is given by

$$\sqrt{\langle \Delta i_{SH}^2 \rangle - \langle \Delta i_{SH} \rangle^2} = \alpha_{LO} \Delta \tilde{X}_w^\phi = \alpha_{LO}, \tag{24}$$

where $\Delta^2 \tilde{X}_w^\phi = \langle (\delta \tilde{X}_w^\phi)^2 \rangle$ is the signal mode ϕ -quadrature variance, and we have used the fact that $\Delta^2 \tilde{X}_w^\phi = \langle (\delta \tilde{X}_w^\phi)^2 \rangle = 1$ for a low noise coherent laser. Clearly, a non-classical squeezed light field can be used to reduce the noise such that $\Delta \tilde{X}_w^{\phi_{LO}} < 1$, however in most cases the resources expended to achieve this outweigh the benefit. Without non classical resources, the signal-to-noise ratio of spatial homodyne detection is therefore limited to

$$\text{SNR}_{SH,coh} = 2\alpha_w(p). \tag{25}$$

Normally, the physically relevant parameter is the sensitivity \mathcal{S} of the detection apparatus, that is the minimum observable change in the parameter p . This is defined as the change in p required to generate a unity signal-to-noise ratio,

$$\mathcal{S}_{SH,coh} = \left[\frac{\partial \text{SNR}}{\partial p} \Big|_{p=0} \right]^{-1} = \frac{1}{2} \left[\frac{\partial \alpha_w(p)}{\partial p} \Big|_{p=0} \right]^{-1}. \tag{26}$$

Equivalently, one finds a SNR for the split detection scheme in the coherent state limit of

$$\text{SNR}_{SD,coh} = 2\alpha_f(p), \tag{27}$$

with a corresponding sensitivity given by

$$S_{SD,coh} = \frac{1}{2} \left[\frac{\partial \alpha_f(p)}{\partial p} \Big|_{p=0} \right]^{-1}. \quad (28)$$

The efficacy of both these detection schemes shall be discussed in the following sections, based on the context in which they are employed. However as we shall demonstrate, the spatial homodyne scheme offers significant improvement over the split detection scheme, and is optimal for all measurements of spatial parameter p .

4. Practical applications 1: Laser beam position measurement

Laser beam position measurement has wide-ranging applications from the macroscopic scale involving the alignment of large-scale interferometers (Fritschel *et al.*, 1998; 2001) and satellites to the microscopic scale involving the imaging of surface structures as encountered in atomic force microscopy (AFM) (Binnig *et al.*, 1985). In an AFM, a cantilever with a nanoscopic-sized tip is scanned across a sample surface, as shown in Fig. 4 (a). The force between the sample surface and tip (e.g. van Der Waals, electrostatic, etc.) results in the tip being modulated spatially as it is scanned across the undulating sample surface. A laser beam is incident on the back of the cantilever with the spatial movement of the cantilever displacing the incident laser beam. The resultant reflected laser beam is detected on a split detector, providing information on the laser position with respect to the centre of the detector, with this information directly related with the AFM tip position. The use of the split detector is ubiquitous in AFM systems.

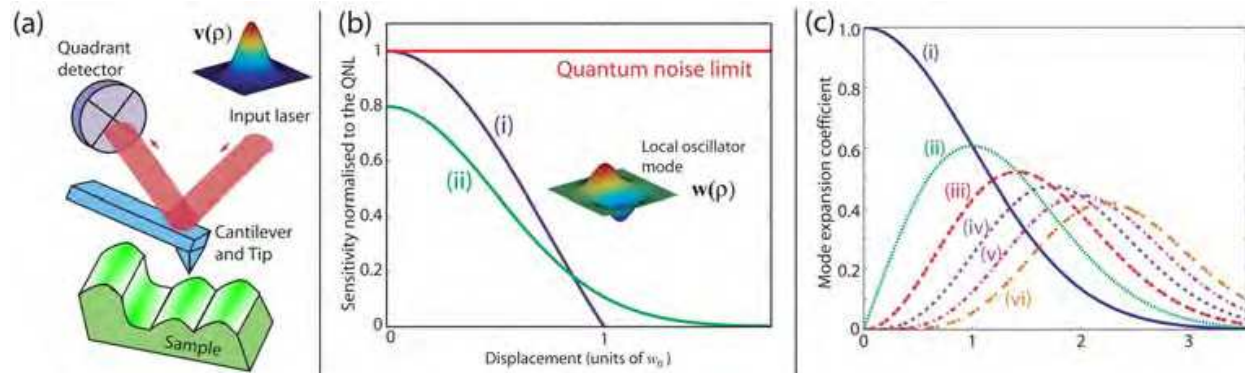


Fig. 4. (a) Schematic diagram illustrating an input field reflected from the back of a cantilever onto a split detector for position sensing of the tip location with respect to a sample. The input laser field has a TEM₀₀ spatial profile, given by $v(\rho)$. (b) Sensitivity of (i) spatial homodyne and (ii) split detection for the measurement of the displacement of a TEM₀₀ input field. The local oscillator field had a TEM₁₀ mode-shape, given by $w(\rho)$. (c) The coefficients of the Taylor expansion of $v(\rho, p)$. The coefficients correspond to the undisplaced (i) TEM₀₀, (ii) TEM₁₀, (iii) TEM₂₀, (iv) TEM₃₀, (v) TEM₄₀, (vi) TEM₅₀ modes. Figures (b) and (c) were reproduced from Hsu *et al.* (2004), with permission.

4.1 Split detection

We now formalise the effects from the application of split detection in determining the AFM tip position. We assume that the laser field incident on the AFM cantilever has a TEM₀₀

modeshape. The spatial information of the displaced field, reflected from the AFM cantilever, is described fully by the field operator given in Eq. (1), now expanded to

$$\tilde{\mathbf{E}}^+(\rho, p) = i\sqrt{\frac{\hbar\omega}{2\epsilon_0 V}} \left(\alpha(p)\mathbf{u}_{00}(\rho, p) + \sum_{m,n=0}^{\infty} \delta\hat{a}_{mn}\mathbf{u}_{mn}(\rho, p) \right), \quad (29)$$

where $\mathbf{u}_{mn}(\rho, p)$ are the transverse beam amplitude functions for the displaced TEM_{mn} modes and $\delta\hat{a}_{mn}$ are the corresponding quantum noise operators. $\alpha(p)$ is the coherent amplitude of the displaced TEM_{00} field. Using the formalism developed in the previous sections, $\mathbf{v}(\rho, p) = \mathbf{u}_{00}(\rho, p)$ and substituting this into Eqs. (15) and (16), gives the normalised difference photocurrent

$$\langle \Delta i_{\text{SD}} \rangle_{d \ll w_0} = \sqrt{\frac{2}{\pi}} \frac{2|\alpha(p)|^2 \tau p}{w_0}, \quad (30)$$

where τ is the measurement time. The difference photo-current is linearly proportional to the displacement p . In the regime where the displacement is assumed to be small (whereby $p \ll w_0$ and w_0 is the waist of the incident laser field), the normalised difference photo-current begins to roll off and asymptotes to a constant for larger p . This can be easily understood, since for $p \gg w_0$ the beam is incident almost entirely on one side of the detector. In this regime, large beam displacements only cause small variations in $\langle \Delta i_{\text{SD}} \rangle$, making it difficult to determine the beam displacement precisely.

For small displacements, the sensitivity of the displacement measurement is found to be given by (Hsu *et al.* (2004))

$$S_{\text{SD}, d \ll w_0} \approx \sqrt{\frac{2}{\pi}} \frac{2|\alpha(p)|\sqrt{\tau}}{w_0}. \quad (31)$$

4.2 Spatial homodyne detection

As discussed earlier, we can use the optimal spatial parameter estimation scheme based on spatial homodyne detection, to detect the beam position in AFM systems. First, the relevant signal mode $\mathbf{w}(\rho)$ of the displaced TEM_{00} input field is identified. A Taylor expansion of the displaced $\mathbf{v}(\rho, p) = \mathbf{u}_{00}(\rho, p)$ input mode provides the relevant displacement signal mode $\mathbf{w}(\rho)$. The coefficients of the Taylor expansion as a function of beam displacement are illustrated in Fig. 4 (c). For small displacements, only the TEM_{00} and TEM_{10} modes have significant non-zero coefficients (Anderson, 1984). This means that for small displacements the TEM_{10} mode contributes most to the displacement signal. For larger displacement, other higher order modes become significant as their coefficients increase. Therefore a spatial homodyne measurement of the displaced TEM_{00} mode using a LO with centred TEM_{10} mode-shape is optimal in the small displacement regime. From Fig. 4 (c), we see that when the input beam is centred, no power is contained in the TEM_{10} mode. Since the Hermite-Gauss modes are orthonormal, the TEM_{10} local oscillator beam only detects the TEM_{10} vacuum noise of the input beam. However as the TEM_{00} beam is displaced, power is coupled into the TEM_{10} mode. This coupled power interferes with the TEM_{10} local oscillator, causing a linear change in the photo-current observed by the homodyne detector.

Using Eq. (1), the electric field operator describing the TEM_{10} local oscillator beam is given by

$$\bar{\mathbf{E}}_{\text{LO}}^+(\rho) = \sqrt{\frac{\hbar\omega}{2\epsilon_0 V}} \left(\alpha_{\text{LO}} \mathbf{u}_{10}(\rho) + \sum_{m,n=0}^{\infty} \delta \hat{a}_{mn}^{\text{LO}} \mathbf{u}_{mn}(\rho) \right) \quad (32)$$

where the first bracketed term is the coherent amplitude which resides in the TEM_{10} mode, the second bracketed term denotes the quantum fluctuations of the beam, and α_{LO} is the coherent amplitude of the LO. The difference photo-current between the two detectors used in the spatial homodyne detection can then be shown from Eqs. (21) to be (Hsu *et al.* (2004))

$$\begin{aligned} \Delta i_{\text{SH}} &= \alpha_{\text{LO}} \left(2p \cdot \frac{\partial[\alpha(p) \mathbf{u}_{00}(\rho, p)]}{\partial p} + \delta \hat{X}_{10}^+ \right) \\ &= \alpha_{\text{LO}} \left(\frac{2|\alpha(p)|^2 \sqrt{\tau}}{w_0} p + \delta \hat{X}_{10}^+ \right) \end{aligned} \quad (33)$$

where $\delta \hat{X}_1^+ = \delta \hat{a}_1 + \delta \hat{a}_1^\dagger$ is the amplitude quadrature noise operator of the TEM_{10} component of the displaced beam, and we have assumed that $\alpha_{\text{LO}} \gg \alpha(p)$.

The spatial homodyne detection sensitivity, obtained in the same manner as that for split detection, is shown in Figure 4 (b). In the small displacement regime, we obtain

$$\mathcal{S}_{\text{SH}, d \ll w_0} = \frac{2|\alpha(p)|\sqrt{\tau}}{w_0} \quad (34)$$

The spatial homodyne detector was shown to be optimal in Section 3.3. Therefore Eq. (34) sets the optimal sensitivity achievable for small displacement measurements. A comparison of the efficiency of split detection for small displacement measurement with respect to the spatial homodyne detector is given by the ratio

$$\epsilon_{\text{SD}} = \frac{\mathcal{S}_{\text{SD}, d \ll w_0}}{\mathcal{S}_{\text{SH}, d \ll w_0}} = \sqrt{\frac{2}{\pi}} \sim 80\%. \quad (35)$$

This $\sqrt{2/\pi}$ factor arises from the coefficient of the mode overlap integral, between $\mathbf{v}(\rho, p) = \mathbf{u}_{00}(\rho, p)$ and $\mathbf{v}_f(\rho, p) = \mathbf{u}_{f00}(\rho, p)$, as shown in Eq. (15), where $\mathbf{u}_{f00}(\rho, p)$ is the flipped TEM_{00} mode. Fig. 4 (b) shows that the maximum sensitivity of split detection is limited at $\sim 80\%$. The sensitivity decreases and asymptotes to zero for large displacement, and is below optimal for all displacement values.

4.3 Using spatial squeezing to enhance measurements for split detection systems

The detection mode arising from the geometry of a split detector is the flipped mode $\mathbf{v}_f(\rho)$. Therefore, in order to perform sub-QNL measurements using a split detector, squeezing of the flipped mode is required. In the case of a quadrant detector, since both horizontal and vertical displacements can be monitored, there exist two detection modes. Therefore, two spatial squeezed modes are required to achieve sub-QNL measurements along two different axes in the transverse plane. An experimental demonstration of simultaneous squeezing for quadrant detection along two different axes in the transverse plane was shown by Treps *et al.* (2003). In their experiment, three beams were required - a bright coherent field with a horizontally phase flipped mode-shape, denoted by TEM_{f00} , and two squeezed fields with TEM_{00} and TEM_{f0f0} (i.e. both phase flipped in the horizontal and vertical axes) mode-shapes,

as shown in Fig. 5 (a). The mode-shape was obtained via the implementation of phase flips on the quadrants in the transverse field. These modes were then overlapped using low finesse, impedance matched optical cavities, with the resulting field imaged onto on a quadrant detector. Measurements of the beam position fluctuations in the horizontal axis were performed by taking the difference between the photocurrents originating from the left and right halves of the quadrant detector. Correspondingly, the beam position fluctuation in the vertical axis were obtained from the difference of the photocurrents from the top and bottom halves of the detector. Treps *et al.* (Treps *et al.*, 2003) demonstrated that simultaneous sub-QNL fluctuations in both horizontal and vertical beam position are obtainable.

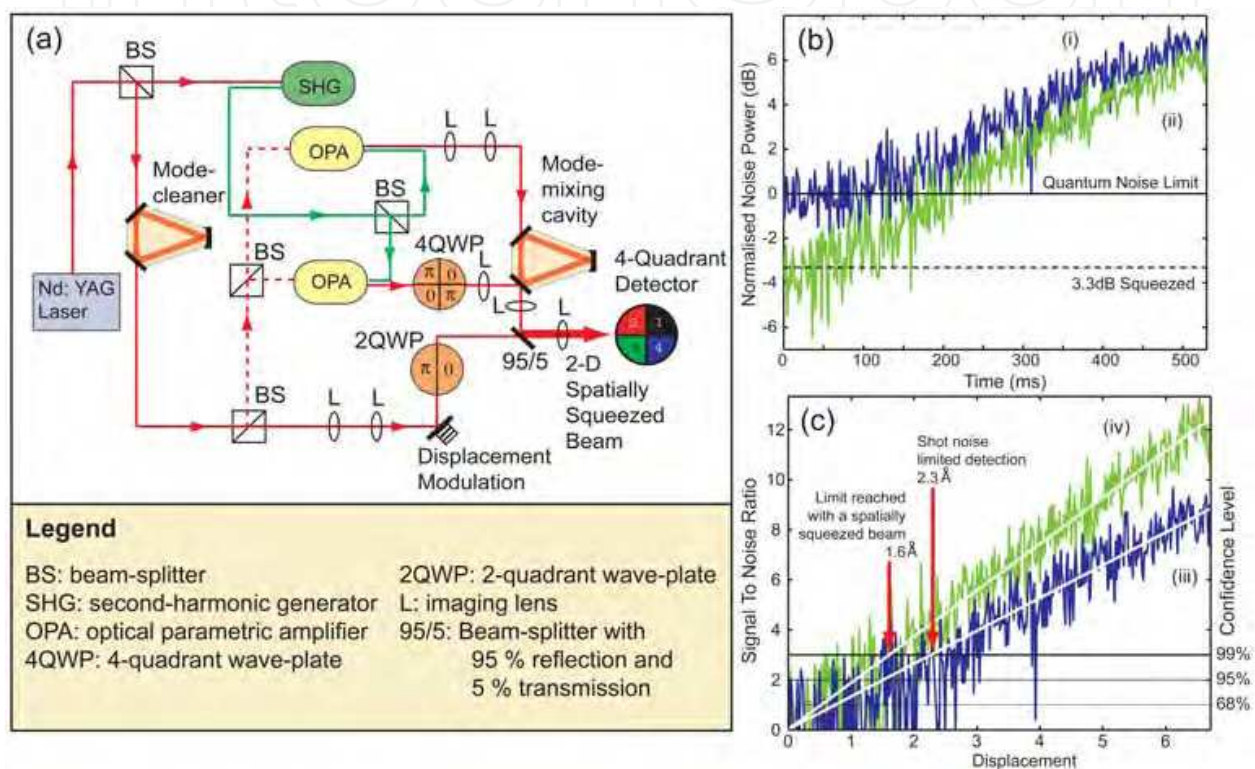


Fig. 5. (a) Schematic of experimental setup for the production of a 2-dimensional spatial squeezed beam for quadrant detection. (b) Measurements of a displacement signal with increasing amplitude in time performed using a beam in the (i) coherent state and (ii) spatially squeezed state. (c) Signal-to-noise ratio (left vertical axis) versus measured displacement. Traces (iii) and (iv) are results obtained from data traces (i) and (ii), respectively. RBW = VBW = 1 kHz, averaged over 20 traces each with detection time $\Delta t = 1$ ms per data point. Figures were reproduced from Treps *et al.* (2002), with permission.

Treps *et al.* (2003) also showed that simultaneous sub-QNL measurements of a displacement signal along two different axes can be produced. A displacement modulation at frequency Ω was applied to the spatially squeezed beam via the use of a mirror mounted on a PZT. The amplitude of the displacement modulation was determined by demodulating the photocurrent at frequency Ω and then measuring the power spectral density, using a spectrum analyser. The measured signal consists of the sum of the squares of the quantum noise with and without applied displacement modulation, given by $p_{\text{mod}}(\Omega)$ and $p_{\text{noise}}(\Omega)$, respectively. For a displacement amplitude modulation that increased with time, the results

of the measurement are shown in Fig. 5 (b). Curve (i) is the result of a displacement measurement performed with a coherent state input beam and sets the classical limit to displacement measurements using quadrant detectors. Curve (ii) is the result of a displacement measurement performed using the spatially squeezed beam.

In order to determine the smallest detectable displacement signal, the results obtained were normalised to the respective noise levels for the coherent and the spatially squeezed beams, shown in Fig. 5 (c). The vertical axis is the signal-to-noise ratio for the displacement measurement. With a 99% confidence level, the smallest detectable displacement is 2.3 Å for a coherent state beam. With the use of the spatially squeezed beam, the smallest detectable displacement was 1.6 Å. Therefore, the spatially squeezed beam provided a factor of 1.5 improvement in the smallest detectable displacement signal, over the coherent state beam.

4.4 Using spatial squeezing to enhance measurements for spatial homodyne detection

Although squeezing of the flipped mode $\mathbf{v}_f(\rho)$ enhances beam displacement measurements on a split detector with sensitivity below the QNL, this scheme remains non-optimal for beam displacement measurements. As shown in previous sections, the QNL for beam displacement measurements is reached in a spatial homodyne detector, assuming the imaging field is in the coherent state. Therefore in order to surpass this QNL, squeezing of the signal mode $\mathbf{w}(\rho)$ responsible for the beam displacement is required. Following the theoretical treatment by Hsu *et al.* (2004), Delaubert *et al.* (2006) performed the first experimental demonstration of squeezing the TEM₁₀ displacement signal mode, for an incident TEM₀₀ beam, followed by displacement signal detection using a TEM₁₀ local oscillator beam in the spatial homodyne detector.

The squeezed TEM₁₀ mode of the incident beam was produced by imaging the squeezed TEM₀₀ output beam from an optical parametric oscillator (OPO) onto a phase mask, as shown in Fig. 6 (a). The phase mask converts the TEM₀₀ squeezed beam into a TEM₁₀ squeezed beam with an efficiency of ~80 %. By using an asymmetric Mach-Zehnder interferometer for combining odd and even-ordered modes, the bright TEM₀₀ beam (i.e. $\mathbf{v}(\rho)$) was combined with the squeezed TEM₁₀ beam (i.e. $\mathbf{w}(\rho)$). The resulting beam was spatially squeezed for optimal detection of small beam displacements. Using a mirror actuated via a PZT, displacement of the beam at RF frequencies was imposed. However, this actuation scheme also introduced a tilt to the beam, therefore the beam was effectively displaced and tilted in the transverse plane, given by

$$\begin{aligned} \mathbf{u}_{00}(\rho, p = d) &= \mathbf{u}_{00}(\rho, 0) + d \cdot \frac{\partial \mathbf{u}_{00}(\rho, 0)}{\partial d} = \mathbf{u}_{00}(\rho, 0) + \frac{d}{w_0} \cdot \mathbf{u}_{10}(\rho, 0) \\ \mathbf{u}_{00}(\rho, p = \theta) &= \mathbf{u}_{00}(\rho, 0) + \theta \cdot \frac{\partial \mathbf{u}_{00}(\rho, 0)}{\partial \theta} = \mathbf{u}_{00}(\rho, 0) + i \frac{\pi \theta w_0}{\lambda} \cdot \mathbf{u}_{10}(\rho, 0) \end{aligned} \quad (36)$$

where d , θ and w_0 are the displacement, tilt and waist of the beam, respectively. The small beam displacement signal is contained in the amplitude quadrature of the TEM₁₀ mode, whilst the small beam tilt signal is contained in the phase quadrature of the TEM₁₀ mode. The displacement and tilt of a beam have been shown to be conjugate observables (Hsu *et al.*, 2005).

The resulting modulated beam was subsequently analysed by interference with a TEM₁₀ local oscillator beam, produced via an optical cavity resonant on the TEM₁₀ mode. Note that

5. Practical applications 2: Particle sensing in optical tweezers

Optical tweezer systems (Ashkin, 1970) have been used extensively for obtaining quantitative biophysical measurements. In particular, particle sensing using optical tweezers provides information on the position, velocity and force of the specimen particles.

A conventional optical tweezers setup is shown in Fig. 7 (a), where a TEM₀₀ trapping field is focused onto a scattering particle. The effective restoring/trapping force acting on the particle is due to two force components: (i) the *gradient force* F_{grad} resulting from the intensity gradient of the trapping beam, which traps the particle transversely toward the high intensity region; and (ii) the *scattering force* F_{scat} resulting from the forward-direction

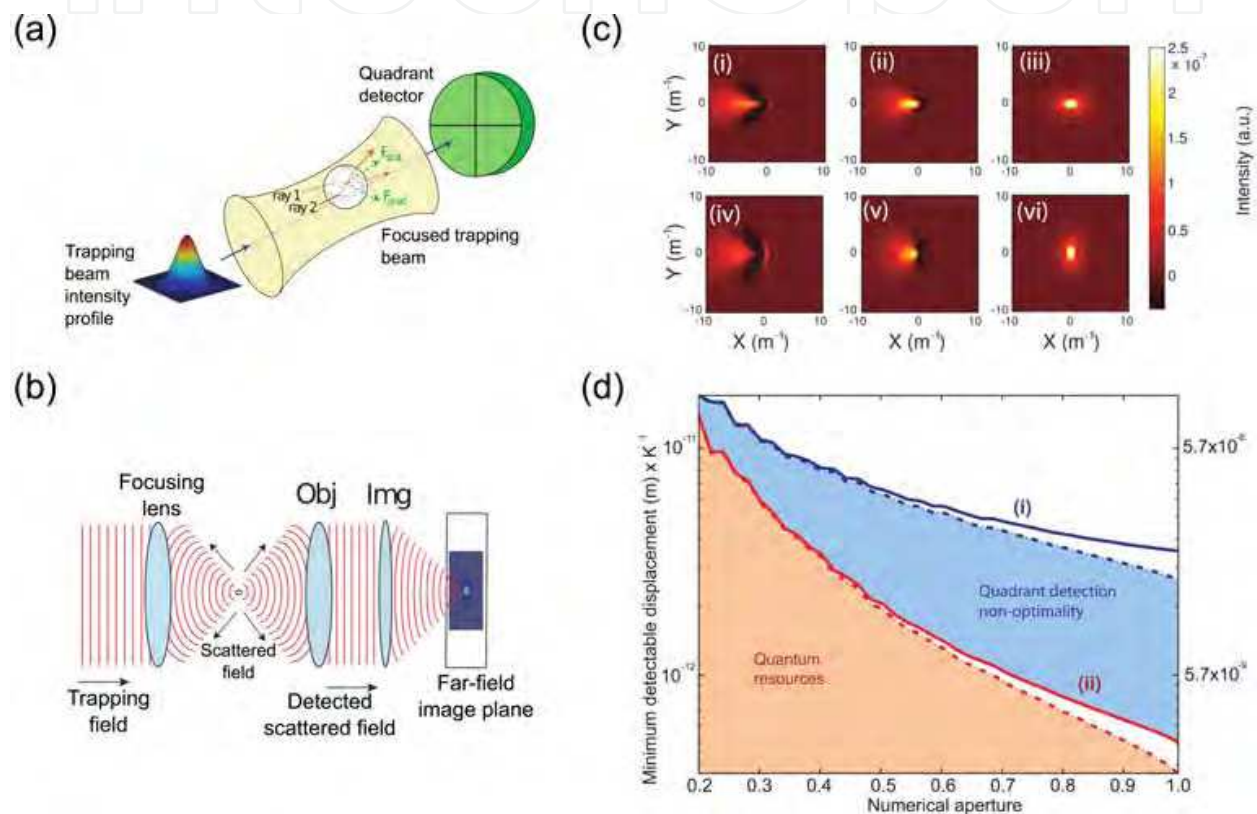


Fig. 7. (a) Illustration showing a TEM₀₀ trapping field focussed onto a spherical scattering particle. The gradient and scattering forces are given by F_{grad} and F_{scat} , respectively. (b) Schematic representation of the trapping and scattered fields in an optical tweezers. The trapping field is incident from the left of the diagram. Obj: objective lens, and Img: imaging lens. (c) Interference pattern of the trapping and forward scattered fields in the far-field plane. Figures (i)-(iii) and (iv)-(vi) assume that the trapping field is x - and y -linearly polarised, respectively. The particle displacements are given by (i), (iv): $1 \mu\text{m}$; (ii), (v): $0.5 \mu\text{m}$; and (iii), (vi): $0 \mu\text{m}$. (d) Minimum detectable displacement normalised by K , versus collection lens NA for (i) split and (ii) spatial homodyne detection. The solid and dashed lines are for x - and y -linearly polarised trapping fields, respectively. The axis on the right shows the minimum detectable displacement assuming 200 mW trapping field power, $\lambda = 1064 \text{ nm}$, particle radius $a = 0.1 \mu\text{m}$, permittivity of the medium $\epsilon_1 = 1$, permittivity of the particle $\epsilon_1 = 3.8$ and trapping field focus of $4 \mu\text{m}$. Absorptive losses in the sample were assumed to be negligible. Figures (b), (c) and (d) were reproduced from Tay *et al.* (2009), with permission.

radiation pressure of the trapping beam incident on the particle. In the focal region of the trapping field, the gradient force dominates over the scattering force, resulting in particle trapping.

To obtain a physical understanding of the trapping forces involved, consider the case with a spherical particle, which has a diameter larger than the trapping field wavelength. Rays 1 and 2 are refracted in the particle, and consequently undergo a momentum change resulting in an equal and opposite momentum change being imparted on the particle. Due to the intensity profile of the beam, the outer ray is less intense than the inner ray which results in the generation of the gradient force (Ashkin, 1992).

If the particle has radius smaller than the wavelength of the trapping laser however, the trapping force is instead generated by an induced dipole moment. In this size regime, the actual shape of the particle is no longer important so long as the particle has no structural deviations greater than the wavelength of the trapping beam. Hence the particle can be treated as a normal dipole with an induced dipole moment along the direction of trapping beam polarisation. The gradient force acting on the particle is then generated due to the interaction of its induced dipole moment with the transverse electromagnetic fields of the trapping field. This force is proportional to the intensity of the beam and has the same net result as before; it acts to return the particle to the centre of the trapping beam focus.

A particle in the beam path will also scatter light. The transverse scattered field profile is dependent on the position of the particle with respect to the centre of the trapping field. By imaging the scattered field onto a position sensitive detector, the position and force of the trapped particle is able to be measured. For these measurements, split detection is most commonly used (Lang & Block, 2003; Gittes & Schmidt, 1998; Pralle *et al.*, 1999), although some direct measurement techniques utilise CCD arrays. To demonstrate the potential enhancement of measurements, we compare split detection and spatial homodyne scheme.

5.1 Modelling

For a single spherical, homogeneous particle with diameter much smaller than the wavelength, the scattered field can be modelled as dipole radiation (Van de Hulst, 1981)². The total field after the objective lens consists of both the scattered and residual trapping fields, given by (Tay *et al.*, 2009)

$$\bar{\mathbf{E}}_{\text{total}}^{\text{I}+}(\rho, p) = \bar{\mathbf{E}}_{\text{scat}}^{\text{I}+}(\rho, p) + \bar{\mathbf{E}}_{\text{trap}}^{\text{I}+}(\rho). \quad (37)$$

where $\bar{\mathbf{E}}_{\text{scat}}^{\text{I}+}(\rho, p)$ and $\bar{\mathbf{E}}_{\text{trap}}^{\text{I}+}(\rho)$ are the respective complex scattered and trapping fields at the image plane. To demonstrate how the changing particle position affected the field at the image plane, Tay *et al.* (2009) calculated the interference between the forward scattered and residual trapping fields for a range of particle displacements in the plane of the trap waist, shown in Fig. 7 (c) for trapping field (i) x - and (ii) y -linearly polarised. Note that the distribution of the field was compressed in the direction of the trapping field polarisation due to dipole scattering along the polarisation axis.

² In the case where there are multiple inhomogeneous particles scattering the input trapping field, several numerical methods exist to calculate the scattered field - e.g. the finite difference frequency domain and T-matrix hybrid method (Loke *et al.*, 2007); and the discrete-dipole approximation and point matching method (Loke *et al.*, 2009).

As before, the critical parameters for assessing sensitivity of particle monitoring are $\alpha(p)$, $\mathbf{v}(\Gamma, p)$ and $\mathbf{w}(\Gamma)$. Using Eq. (6) we obtain

$$\begin{aligned}\mathbf{v}(\Gamma, p) &= -iN_v \bar{\mathbf{E}}_{\text{total}}^{\text{I}+}(\Gamma, p) \\ &= -i\sqrt{\frac{2\epsilon_0 V}{\hbar\omega}} \frac{1}{\alpha_{\text{trap}}} \left(\bar{\mathbf{E}}_{\text{scat}}^{\text{I}+}(\Gamma, p) + \bar{\mathbf{E}}_{\text{trap}}^{\text{I}+}(\Gamma) \right),\end{aligned}\quad (38)$$

where α_{trap} is the coherent amplitude of the trapping field. Now using Eq. (9) the functional form for the mode that contains information about the particle position is given by

$$\mathbf{w}(\Gamma) = -iN_w \left. \frac{\partial \bar{\mathbf{E}}_{\text{scat}}^{\text{I}+}(\Gamma, p)}{\partial p} \right|_{p=0}.\quad (39)$$

Note that this mode is only dependent on the scattered field.

It is then possible to calculate the SNR of the spatial homodyne and split detection schemes for particle sensing in an optical tweezers arrangement. By substituting the expressions obtained in Eq. (39) into Eq. (25), the SNR for the spatial homodyne detection scheme is given by

$$\begin{aligned}\text{SNR}_{\text{SH,coh}} &= -2i\sqrt{\frac{2\epsilon_0 V}{\hbar\omega}} \int_{-\infty}^{\infty} \mathbf{w}(\Gamma)^* \cdot \bar{\mathbf{E}}_{\text{scat}}^{\text{I}+}(\Gamma, p) d\Gamma \\ &= -2K\sqrt{2V} \int_{-\infty}^{\infty} \mathbf{w}(\Gamma)^* \cdot \mathbf{A}(\Gamma) d\Gamma,\end{aligned}\quad (40)$$

where the image plane co-ordinates are given by Γ and

$$K = \alpha_{\text{trap}} k^2 a^3 \left(\frac{\epsilon_1 - \epsilon_2}{\epsilon_1 + 2\epsilon_2} \right),\quad (41)$$

where ϵ_1 and ϵ_2 are the respective permittivity of the medium and particle; and a is the radius of the particle. In a similar manner, using Eq. (27), the SNR for the split detection scheme is given by

$$\text{SNR}_{\text{SD,coh}} = -2K\sqrt{2V} \int_{-\infty}^{\infty} \mathbf{v}_f(\Gamma)^* \cdot \mathbf{A}(\Gamma) d\Gamma.\quad (42)$$

Correspondingly, the sensitivities for the spatial homodyne and split detection schemes can be calculated using Eqs. (26) and (28), respectively. The explicit forms for these expressions can be found in Tay *et al.* (2009).

5.2 Results

The performance of both split and spatial homodyne detection schemes were compared by considering the sensing of particle displacement from the centre of the optical tweezers trap (Tay *et al.*, 2009). The SNR for (a) split; and spatial homodyne detection in the (b) small and (c) large displacement regimes are shown in Fig. 8. It was found that the SNR for spatial homodyne detection was maximised at different particle displacement regimes depending on the LO mode used.

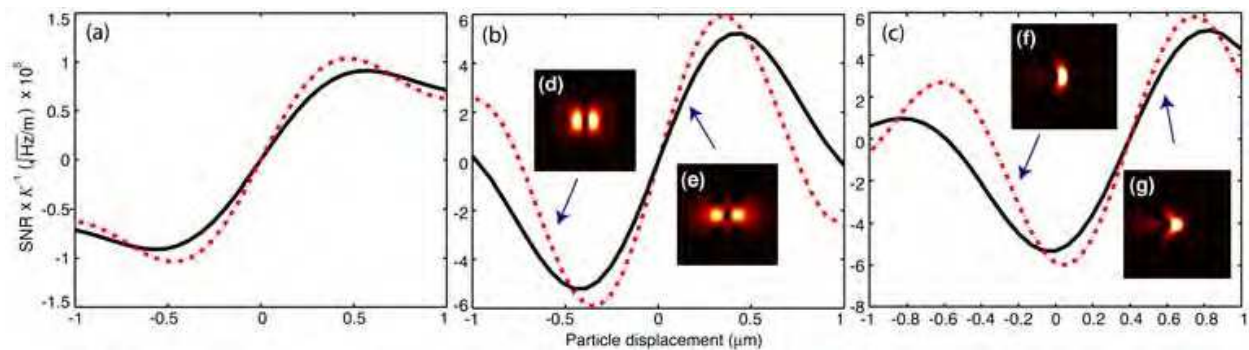


Fig. 8. SNR normalised to K versus particle displacement with respect to the centre of the trapping field, for (a) split detection; (b) spatial homodyne detection with LO spatial mode optimised for small displacement measurements; and (c) spatial homodyne detection with LO spatial mode optimised for larger displacement measurements. The black solid and red dashed lines are for x - and y -linearly polarised trapping fields, respectively. The corresponding LO spatial modes are the inset figures with (d) y - and (e) x -linearly polarised trapping fields for the small displacement regime. For the large displacement regime, the LO spatial modes are correspondingly: (f) y - and (g) x -linearly polarised trapping fields. Model parameters are 200 mW trapping field power, $\lambda = 1064$ nm, particle radius $a = 0.1$ μm , permittivity of the medium $\epsilon_1 = 1$, permittivity of the particle $\epsilon_1 = 3.8$ and trapping field focus of 4 μm . Absorptive losses in the sample were assumed to be negligible. Figures were reproduced from Tay *et al.* (2009), with permission.

Assuming small displacements, the LO field was determined from the first order term in the Taylor expansion of Eq. (9) for the scattered field, with the SNR given in Fig. 8 (b). For particle displacements less than the trapping beam waist, linearity of the SNR was obtained. Optimum sensitivity (i.e. the maximum SNR slope) occurred at zero displacement and surpassed the maximum of split detection by almost an order of magnitude. However, for particle displacements $\sim |0.4|$ μm , the SNR peaked, indicating that small displacements of a particle around $\sim |0.4|$ μm are not resolvable using the current LO mode. As the particle was displaced further, a drop in the total scattered power was observed due to the particle moving out of the trapping field, resulting in an exponential decay of the SNR. To re-optimize the LO mode for particle displacement around any arbitrary position, a Taylor expansion in p of the scattered field can be taken at that position while only retaining the first order term. For example, for particles fluctuating around $\sim |0.4|$ μm , the re-optimised LO mode resulted in the SNR given in Fig. 8 (c) where the maximum SNR slope was now located around $\sim \pm 0.4$ μm . Therefore, it is possible to dynamically adjust the LO mode to optimize the measurement sensitivity whilst the particle moves, resulting in optimum particle sensing for all displacement values.

The corresponding sensitivities for (i) split and (ii) spatial homodyne detection as a function of increasing objective lens NA are shown in Fig. 7 (d). It was observed that the minimum detectable displacement for both split and spatial homodyne detection decreased with increasing NA due to more scattered field being collected, thereby providing more information about the particle position. However, spatial homodyne detection outperforms split detection for all NA values, since spatial homodyne optimally extracts the displacement information from the detected field, whereas the split detection scheme only measures partial displacement information, as shown in Eq. (15). Due to the optimal signal

and noise measurement using the spatial homodyne scheme, curve (ii) defines the minimum detectable displacement in optical tweezers systems.

To provide quantitative values for the minimum detectable displacement, the sensitivities for both detection schemes using realistic experimental values are shown in the right-hand side axis of Fig. 7 (d). The *split detection non-optimality* shaded area shows the loss in particle sensing sensitivity due to incomplete mode detection from a split detector. The *quantum resources* shaded area shows that quantum resources such as spatial squeezed light (Treppe *et al.*, 2002; 2003) can be used to further enhance the particle sensing sensitivity beyond the QNL.

The ability to tailor the local oscillator mode provides tremendous optimisation ability for particle sensing. Not only is optimal information extraction possible, but it is now possible to perform sensing of multiple inhomogeneous particles, with information extraction of any spatial parameter p , via the modification of the LO mode.

6. Conclusion

We have presented a quantum formalism for the measurement of the spatial properties of an optical field. It was shown that the spatial homodyne technique is optimal and outperforms split detection for the detection of spatial parameter p . Applications of this measurement scheme in enhancing the sensitivities of atomic force microscopes and optical tweezers measurements have been discussed.

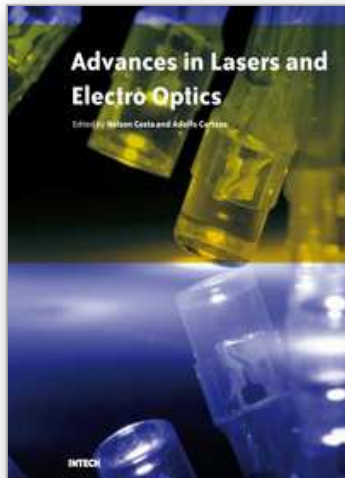
7. References

- Anderson, D. Z. (1984). Alignment of resonant optical cavities. *Appl. Opt.*, Vol. 23, No. 17, 2944-2949.
- Arnon, S. (1998). Use of satellite natural vibrations to improve performance of free-space satellite laser communication. *Appl. Opt.*, Vol. 37, 5031.
- Ashkin, A. (1992). Forces of a single-beam gradient laser trap on a dielectric sphere in the ray optics regime. *Biophys. J.*, Vol. 61, No. 2, 569-582.
- Ashkin, A. (1970). Acceleration and Trapping of Particles by Radiation Pressure. *Phys. Rev. Lett.*, Vol. 24, No. 4, 156-159.
- Beck M. (2000). Quantum state tomography with array detectors *Phys. Rev. Lett.*, Vol. 84, No. 25, 5748.
- Binnig, G.; Quate, C. F.; and Gerber, Ch. (1985). Atomic Force Microscope. *Phys. Rev. Lett.*, Vol. 56, No. 9, 930-933.
- Block S. M. (1992). Making light work with optical tweezers *Nature*, Vol. 360, 493-495.
- Born M. and Wolf E. *Principles of Optics* (Cambridge University Press, Cambridge, UK, 1999)
- Bowen W. P., Schnabel R., Bachor H.-A. , and Lam P. K. (2002). Polarization squeezing of continuous variable stokes parameters. *Physical Review Letters* Vol. 88, 093601.
- Dawes, A.M.; Beck, M.; and Banaszek, K. (2003). Mode optimization for quantum-state tomography with array detectors. *Phys. Rev. A.*, Vol. 67, 032102.
- Dawes, A.M.; and Beck, M. (2001). Simultaneous quantum-state measurements using array detection. *Phys. Rev. A.*, Vol. 63, 040101(R).
- Delaubert, V., Treppe, N., Harb, C. C., Lam, P. K., and Bachor, H.-A. (2006). Quantum measurements of spatial conjugate variables: displacement and tilt of a Gaussian beam. *Opt. Letts.*, Vol. 31, No. 10, 1537-1539.

- Delaubert, V.; Treps, N.; Fabre, C.; Bachor, H.-A.; and Réfrégier, P. (2008). Quantum limits in image processing. *Europhys. Lett.*, Vol. 81, 44001.
- Fabre, C.; Fouet, C. J.; and Maître, A. (2000). Quantum limits in the measurement of very small displacements in optical images. *Opt. Lett.*, Vol. 25, pp. 76.
- Fritschel, P.; Mavalvala, N.; Shoemaker, D.; Sigg, D.; Zucker, M.; and González, G. (1998). Alignment of an interferometric gravitational wave detector. *Appl. Opt.*, Vol. 37, No. 28, 6734-6747.
- Fritschel, P.; Bork, R.; González, G.; Mavalvala, N.; Ouimette, D.; Rong, H.; Sigg, D.; and Zucker, M. (2001). Readout and Control of a Power-Recycled Interferometric Gravitational-Wave Antenna. *Appl. Opt.*, Vol. 40, No. 28, 4988-4998.
- Gittes, F.; and Schmidt, C. F. (1998). Interference model for back-focal-plane displacement detection in optical tweezers. *Opt. Lett.* Vol. 23, No. 1, 7-9.
- Hell, S.W.; Schmidt, R.; and Egner, A. (2009). Diffraction-unlimited three-dimensional optical nanoscopy with opposing lenses *Nature Photonics* 3, 381-387.
- Hsu, M. T. L.; Delaubert, V.; Lam, P. K.; and Bowen, W. P. (2004). Optimal optical measurement of small displacements. *Journal of Optics B: Quantum and Semiclassical Optics*, Vol. 6, No. 12, 495-501.
- Hsu, M. T. L.; Bowen, W. P.; Treps, N.; and Lam, P. K. (2005). Continuous-variable spatial entanglement for bright optical beams. *Phys. Rev. A*, Vol. 72, No. 1, 013802.
- Hsu, M. T. L.; Bowen, W. P. and Lam, P. K. (2009). Spatial-state Stokes-operator squeezing and entanglement for optical beams. *Physical Review A*, Vol. 79, No. 4, 043825.
- Korolkova, N. V.; and Chirkin, A. S. (1996). Formation and conversion of the polarization-squeezed light. *Journal of Modern Optics*, Vol. 43, issue 5, 869-878.
- Lang, M. J.; and Block, S. M. (2003). LBOT-1: Laser-based optical tweezers. *Am. J. Phys.*, Vol. 71 No. 3, 201-215; and references therein.
- Loke, V. L. Y.; Nieminen, T. A.; Parkin, S. W.; Heckenberg, N. R.; and Rubinsztein-Dunlop, H. (2007). FDFD/T-matrix hybrid method. *J. Quant. Spec. Rad. Trans.*, Vol. 106, No. 1, 274-284.
- Loke, V. L. Y.; Nieminen, T. A.; Heckenberg, N. R.; and Rubinsztein-Dunlop, H., J. (2009). T-matrix calculation via discrete dipole approximation, point matching and exploiting symmetry. *Quant. Spec. Rad. Trans.*, Vol. 110, No. 14, 1460-1471.
- Mach, L. (1892). *Z. Instrumentenkunde* 12, 89.
- Nikulin, V. V.; Bouzoubaa, M.; Skormin, V. A.; and Busch, T. E. (2001). Modeling of an acousto-optic laser beam steering system intended for satellite communication. *Opt. Eng.*, Vol. 40, 2208.
- Pawley J. (1995). *Handbook of Biological Confocal Microscopy*, Springer, Germany.
- Pendry, J. B. (2000). Negative refraction makes a perfect lens. *Phys. Rev. Lett.* , Vol. 85, No. 14, 3966-3969.
- Pralle, A.; Prummer, M.; Florin, E.-L.; Stelzer, E. H. K.; and Hörber, J. K. H. (1999). Threedimensional high-resolution particle tracking for optical tweezers by forward scattered light. *Microsc. Res. Tech.*, Vol. 44, No. 5, 378-386.
- Putman, C. A.; De Grooth, B. G.; Van Hulst, N. F.; and Greve, J. (1992). A detailed analysis of the optical beam deflection technique for use in atomic force microscopy. *J. Appl. Phys.*, Vol. 72, No. 1, 6.
- Sagnac, G. (1912). L'éther lumineux démontré par l'effet du vent relatif d'éther dans un interféromètre en rotation uniforme. *Comptes Rendus* 157 (1913), S. 708-710

- Saleh, B. E. A.; and Teich, M. C. (1991). *Fundamentals of Photonics*, JohnWiley and Sons, New York.
- Shaddock, D. A.; Gray, M. B.; and McClelland, D. E., (1999). Frequency locking a laser to an optical cavity by use of spatial mode interference. *Opt. Lett.*, Vol. 24, No. 21, pp. 1499-1501.
- Slusher, R. E.; Hollberg, L. W.; Yurke, B.; Mertz, J. C.; and Valley, J. F. (1985). Observation of Squeezed States Generated by Four-Wave Mixing in an Optical Cavity, *Phys. Rev. Lett.*, Vol. 55, No. 22, 2409-2412.
- Synge, E. H. (1928). A suggested method for extending the microscopic resolution into the ultramicroscopic region. *Phil. Mag.* 6, 356.
- Tay, J. W.; Hsu, M. T. L.; and Bowen, W. P. (2009). Quantum limited particle sensing in optical tweezers. e-print arXiv:0907.4198
- Treps, N.; Andersen, U.; Buchler, B.; Lam, P. K.; Maître, A.; Bachor, H.-A.; and Fabre, C. (2002). Surpassing the Standard Quantum Limit for Optical Imaging Using Nonclassical Multimode Light. *Phys. Rev. Lett.*, Vol. 88, No. 20, 203601 (2002).
- Treps, N., Grosse, N.; Bowen, W. P.; Fabre, C.; Bachor, H.-A.; and Lam, P. K. (2003). A Quantum Laser Pointer. *Science.*, Vol. 301, No. 5635, 940-943. See also: Treps, N.; Grosse, N.; Bowen, W. P.; Hsu, M. T. L.; Maître, A.; Fabre, C.; Bachor, H.-A.; and Lam, P. K. (2004). Nano-displacement measurements using spatially multimode squeezed light. *J. Opt. B: Quantum Semiclass.*, Vol. 6, No. 8, S664-S674.
- Treps, N.; Delaubert, V.; Maître A.; Courty, J.M.; Fabre, C. (2005). Quantum noise in multipixel image processing. *Phys. Rev. A*, Vol. 71, No. 1, 013820.
- Van De Hulst, H. C. (1981). *Light Scattering by Small Particles*. Dover Publications, ISBN:0486642283, New York. See also: Berne, B. J., and R. Pecora. (2000). *Dynamic Light Scattering*. Dover Publications, ISBN:0486411559, New York.
- Walls, D. F.; and Milburn, G. J. (1995). *Quantum Optics*, Springer, Germany. Zehnder, L. (1891). *Z. Instrumentenkunde* 11, 275.

IntechOpen



Advances in Lasers and Electro Optics

Edited by Nelson Costa and Adolfo Cartaxo

ISBN 978-953-307-088-9

Hard cover, 838 pages

Publisher InTech

Published online 01, April, 2010

Published in print edition April, 2010

Lasers and electro-optics is a field of research leading to constant breakthroughs. Indeed, tremendous advances have occurred in optical components and systems since the invention of laser in the late 50s, with applications in almost every imaginable field of science including control, astronomy, medicine, communications, measurements, etc. If we focus on lasers, for example, we find applications in quite different areas. We find lasers, for instance, in industry, emitting power level of several tens of kilowatts for welding and cutting; in medical applications, emitting power levels from few milliwatt to tens of Watt for various types of surgeries; and in optical fibre telecommunication systems, emitting power levels of the order of one milliwatt. This book is divided in four sections. The book presents several physical effects and properties of materials used in lasers and electro-optics in the first chapter and, in the three remaining chapters, applications of lasers and electro-optics in three different areas are presented.

How to reference

In order to correctly reference this scholarly work, feel free to copy and paste the following:

Warwick P. Bowen, Magnus T. L. Hsu and Jian Wei Tay (2010). Fundamentals and Applications of Quantum Limited Optical Imaging, *Advances in Lasers and Electro Optics*, Nelson Costa and Adolfo Cartaxo (Ed.), ISBN: 978-953-307-088-9, InTech, Available from: <http://www.intechopen.com/books/advances-in-lasers-and-electro-optics/fundamentals-and-applications-of-quantum-limited-optical-imaging>

INTECH
open science | open minds

InTech Europe

University Campus STeP Ri
Slavka Krautzeka 83/A
51000 Rijeka, Croatia
Phone: +385 (51) 770 447
Fax: +385 (51) 686 166
www.intechopen.com

InTech China

Unit 405, Office Block, Hotel Equatorial Shanghai
No.65, Yan An Road (West), Shanghai, 200040, China
中国上海市延安西路65号上海国际贵都大饭店办公楼405单元
Phone: +86-21-62489820
Fax: +86-21-62489821

© 2010 The Author(s). Licensee IntechOpen. This chapter is distributed under the terms of the [Creative Commons Attribution-NonCommercial-ShareAlike-3.0 License](https://creativecommons.org/licenses/by-nc-sa/3.0/), which permits use, distribution and reproduction for non-commercial purposes, provided the original is properly cited and derivative works building on this content are distributed under the same license.

IntechOpen

IntechOpen